Journal of Materials Chemistry B

ROYAL SOCIETY OF CHEMISTRY

PAPER

View Article Online
View Journal | View Issue

Cite this: J. Mater. Chem. B, 2023, 11, 6595

Nanozyme-integrated microneedle patch for enhanced therapy of cutaneous squamous cell carcinoma by breaking the gap between H_2O_2 self-supplying chemodynamic therapy and photothermal therapy†

Enguo Ju, ‡[a] Mengran Peng,‡[a] Yanteng Xu,[a] Yuqin Wang,[a] Feng Zhou,[a] Haixia Wang,[a] Mingqiang Li,[ab] Yue Zheng*[a] and Yu Tao*[a]

Received 31st March 2023,
Accepted 23rd May 2023

DOI: 10.1039/d3tb00708a

rsc.li/materials-b

Cutaneous squamous cell carcinoma (cSCC) is one of the most common skin cancers with increasing incidence worldwide. However, it is still challenging to prevent the relapse of cSCC due to poor drug penetration across the stratum corneum. Herein, we report the design of a microneedle patch loaded with MnO_2/Cu_2O nanosheets and combretastatin A4 (MN-MnO_2/Cu_2O-CA4) for the enhanced therapy of cSCC. The prepared MN-MnO_2/Cu_2O-CA4 patch could effectively deliver adequate drugs locally into the tumor sites. Moreover, the glucose oxidase (GOx)-mimicking activity of MnO_2/Cu_2O could catalyze glucose to produce H_2O_2, which combined with the released Cu to induce a Fenton-like reaction to efficiently generate hydroxyl radicals for chemodynamic therapy. Meanwhile, the released CA4 could inhibit cancer cell migration and tumor growth by disrupting the tumor vasculature. Moreover, MnO_2/Cu_2O was endowed with the ability of photothermal conversion under the irradiation of near-infrared (NIR) laser, which could not only kill the cancer cells but also promote the efficiency of the Fenton-like reaction. Significantly, the photothermal effect did not compromise the GOx-like activity of MnO_2/Cu_2O, which guaranteed enough production of H_2O_2 for the sufficient generation of hydroxyl radicals. This work may open avenues for constructing MN-based multimodal treatment for the efficient therapy of skin cancers.

1. Introduction

As the second most common non-melanoma skin cancer after basal cell carcinoma, cutaneous squamous cell carcinoma (cSCC) is an epidermal keratinocyte-derived skin tumor, which accounts for 20% of all skin cancer-related deaths.[1] Risk factors, including ultraviolet radiation, age, fair skin pigmentation, and immunosuppression, represent a strong relationship with cSCC.[2] Although surgery with improved survival is the mainstay of curative treatment, cancer recurrence and metastasis remain the leading cause of treatment failure after surgical resection.[3] Some histologic subtypes of cSCC, such as the desmoplastic variant and adenosquamous variant, contribute to a high risk of local recurrence and metastasis.[4,5] Moreover, surgery is not suitable for the elderly patients on immunosuppressants or

[a] Laboratory of Biomaterials and Translational Medicine, Center for Nanomedicine, Department of Dermato-Venereology, The Third Affiliated Hospital, Sun Yat-sen University, Guangzhou 510630, China. E-mail: zhengy58@mail.sysu.edu.cn, taoy28@mail.sysu.edu.cn

[b] Guangdong Provincial Key Laboratory of Liver Disease Research, Guangzhou 510630, China

† Electronic supplementary information (ESI) available. See DOI: https://doi.org/10.1039/d3tb00708a

‡ These authors contributed equally to this work.

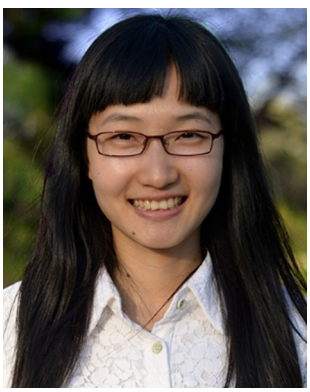

Yu Tao

Yu Tao is Professor at Sun Yat-sen University. She obtained her BS degree from Nanjing Normal University in 2009 and received her PhD degree in Inorganic Chemistry and Chemical Biology from the Chinese Academy of Sciences in 2015. Then she did postdoctoral training at the City College of New York and Columbia University from 2015 to 2018. Her research interests include biomaterials, nanotechnology, and tissue engineering.

anticoagulants. In addition, for cSCC located on the eyelid, lip, or ear with the requirement of maximum tissue preservation, surgery may result in poor cosmetic outcomes. Nonsurgical approaches, such as cryotherapy, imiquimod, and 5-fluorouracial, come with poor outcomes and high recurrence rates.[6] Recently, topical photodynamic therapy has been applied for the treatment of certain nonmelanoma skin cancers owing to its safety, easy access, and good cosmetic outcome.[7] However, the efficacy is limited by the inadequate penetration of topically applied photosensitizer through the keratinized tumor surface and insufficient local bioavailability.[8] Therefore, it is critical to develop new strategies to improve the therapeutic benefits.

As an emerging therapeutic strategy, chemodynamic therapy has attracted considerable attention through the *in situ* initiation of a Fenton reaction or Fenton-like reaction to generate hydroxyl radicals, which inhibit tumor growth.[9] Meanwhile, considerable efforts have been devoted to enhancing the therapeutic efficacy by combining chemodynamic therapy with other treatment modalities, such as photothermal therapy, which can generate heat to promote the efficiency of the Fenton reaction.[10,11] However, one critical issue is how to produce enough H_2O_2 to generate sufficient hydroxyl radicals for tumor suppression.[12] To solve this problem, various materials, including CaO_2, CuO_2, and ZnO_2, have been applied to achieve the self-supply of H_2O_2.[13–16] Despite being promising, their low stability in an aqueous environment has become a major concern for clinical application. Another approach is the use of glucose oxidase (GOx) to catalyze the oxidization of intracellular glucose to produce large amounts of H_2O_2. However, the short *in vivo* half-life, immunogenicity, and systemic toxicity hinders the applications of natural enzymes.[17] Moreover, the high-temperature environment induced by photothermal therapy would greatly decrease the enzymatic activity of GOx.[18] Nanozymes with GOx-like activity hold great potential in producing self-supplying H_2O_2 due to their high stability and the maintenance of activity over broad ranges of temperature.[19–21] Therefore, it is highly desirable to integrate nanozymes into the construction of therapeutics to bridge the gap between the self-supplied H_2O_2 chemodynamic therapy and photothermal therapy.

Herein, we report the design of a microneedle patch loaded with MnO_2/Cu_2O nanosheets and combretastatin A4 (MN-MnO_2/Cu_2O-CA4) for the therapy of cSCC (Scheme 1). The encapsulation of MnO_2/Cu_2O and CA4 into the microneedles ensures the delivery of adequate drug to the tumor sites. In addition, the GOx-mimicking activity of MnO_2/Cu_2O could catalyze glucose to produce H_2O_2, which combined with the released Cu and induces the Fenton-like reaction to efficiently generate hydroxyl radicals for efficient chemodynamic therapy. Moreover, the photothermal conversion property of MnO_2/Cu_2O could not only kill the cancer cells but also promote the efficiency of the Fenton-like reaction. It is important to note that the GOx-mimicking activity of MnO_2/Cu_2O does not get compromised with high temperature. In addition, the released CA4, as a vascular disrupting agent, could inhibit cancer cell migration and tumor growth. This study may provide a strategy for constructing MN-based multimodal treatment for the enhanced therapy of cSCC.

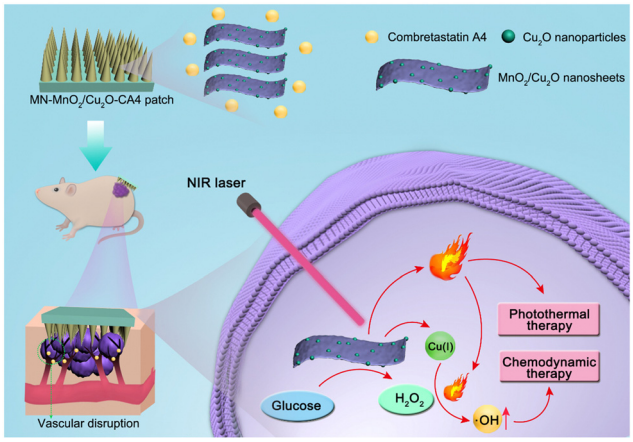

Scheme 1 Schematic illustration of MN-MnO_2/Cu_2O-CA4 patch for synergistic photothermal and chemodynamic therapy of cutaneous squamous cell carcinoma.

2. Results and discussion

First, MnO_2 nanosheets were synthesized *via* a wet-chemical method as previously reported.[18] Thereafter, Cu_2O nanoparticles were deposited on the MnO_2 nanosheets to form MnO_2/Cu_2O nanosheets (Fig. 1A).[22] The hydrodynamic size of the MnO_2

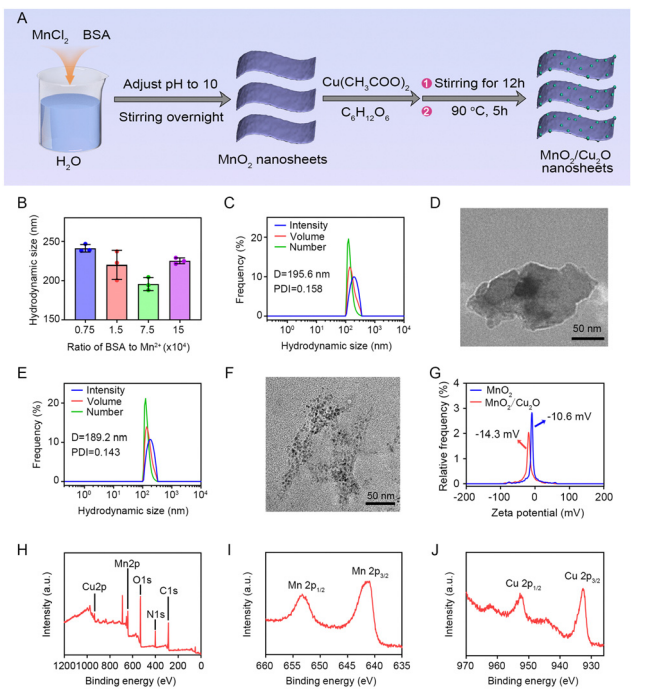

Fig. 1 Synthesis and characterization of MnO_2/Cu_2O nanosheets. (A) Schematic illustration of the synthesis of MnO_2/Cu_2O nanosheets. (B) Hydrodynamic size of MnO_2 nanosheets prepared from different ratios of BSA to $MnCl_2$. (C) Hydrodynamic size of MnO_2 nanosheets with the ratio of BSA to $MnCl_2$ of 7.5×10^4:1. (D) TEM image of MnO_2 nanosheets. (E) Hydrodynamic size of MnO_2/Cu_2O nanosheets. (F) TEM image of MnO_2/Cu_2O nanosheets. (G) Zeta potential of MnO_2 and MnO_2/Cu_2O nanosheets. (H) XPS spectra of MnO_2/Cu_2O nanosheets. (I and J) High-resolution XPS spectra of Mn2p (I) and Cu2p (J).

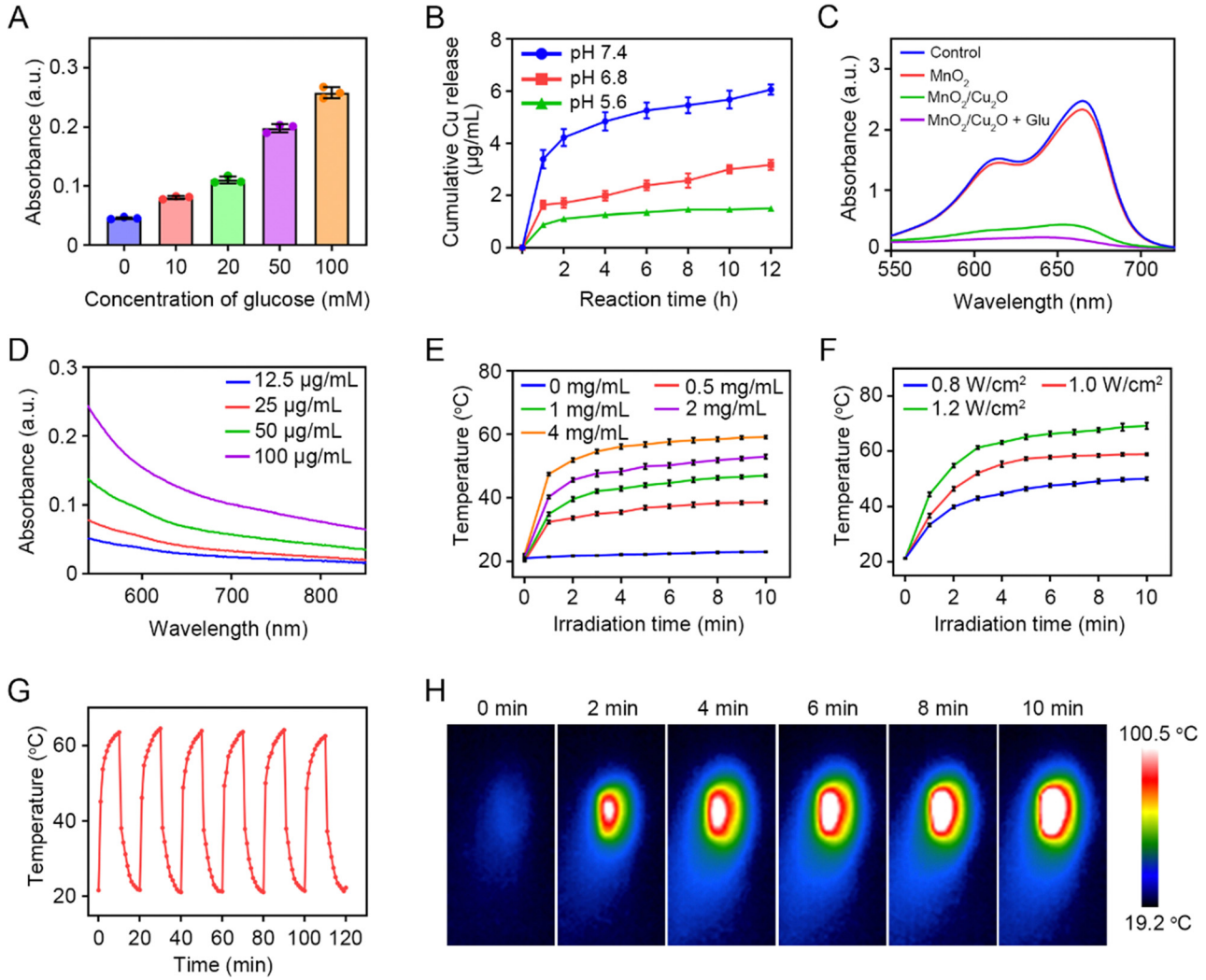

Fig. 2 Investigation of the GOx activity, copper ion release, ROS generation, and photothermal effect of MnO_2/Cu_2O nanosheets. (A) The absorbance value at 650 nm to measure the GOx activity of MnO_2/Cu_2O in the presence of glucose, HRP, and TMB. (B) Detection of the released copper ions from MnO_2/Cu_2O nanosheets at different pH by employing sodium diethyldithiocarbamate trihydrate. (C) Methylene blue degradation assay to determine the generation of hydroxyl radicals in the presence of H_2O_2. (D) Absorbance spectrum of MnO_2/Cu_2O nanosheets. (E) Temperature of MnO_2/Cu_2O solution with various concentrations under NIR laser irradiation. (F) Temperature of MnO_2/Cu_2O solution with indicated laser powers. (G) Temperature variation of MnO_2/Cu_2O solution over six cycles of NIR laser on/off irradiation. (H) Thermal images of MnO_2/Cu_2O solution with the irradiation of NIR laser.

nanosheets varied with the ratio of BSA to Mn^{2+} (Fig. 1C). MnO_2 prepared with the molar ratio of BSA to Mn^{2+} of 7.5×10^4:1 was chosen due to the relatively small size and polydisperse index (Fig. 1B). Transmission electron microscopy (TEM) images confirmed the sheet-like shape of MnO_2 (Fig. 1D). After Cu_2O was deposited on the MnO_2 nanosheets, the hydrodynamic size of MnO_2/Cu_2O was comparable to that of MnO_2 (Fig. 1E). Besides, TEM images showed numerous dark dots on the gray sheet, which indicated the successful synthesis of MnO_2/Cu_2O (Fig. 1F). Besides, the zeta potential of MnO_2 changed from −10.6 mV to −14.3 mV as a result of Cu_2O deposition (Fig. 1G). In addition, the synthesized MnO_2/Cu_2O showed good colloidal stability. This may be attributed to the reason that BSA not only acted as nucleation sites for both Mn and Cu in this synthetic process, but also as the protective agent to increase the solubility and stability.

To determine the elemental composition and chemical bonding of the MnO_2/Cu_2O nanosheets, X-ray photoelectron spectroscopy (XPS) was performed. As shown in Fig. 1H, MnO_2/Cu_2O nanosheets were mainly composed of C, O, N, Mn, and Cu. The high-resolution XPS curve of Mn2p exhibited two peaks at around 641.28 eV and 653.28 eV, which confirmed the +4 valence state of Mn (Fig. 1I). In addition, two peaks at 932.38 eV and 952.78 eV with satellites were observed in the high-resolution XPS spectra of Cu2p, which indicated that the valence state of Cu was +1 in the prepared MnO_2/Cu_2O nanosheets (Fig. 1J).

A previous study reported that the BSA-templated MnO_2 displayed GOx-like activity, and based on this, we evaluated the GOx activity of MnO_2/Cu_2O by detecting the produced H_2O_2 using the HRP-catalyzed oxidation of a TMB system. As shown in Fig. 2A, MnO_2/Cu_2O successfully catalyzed the oxidation of

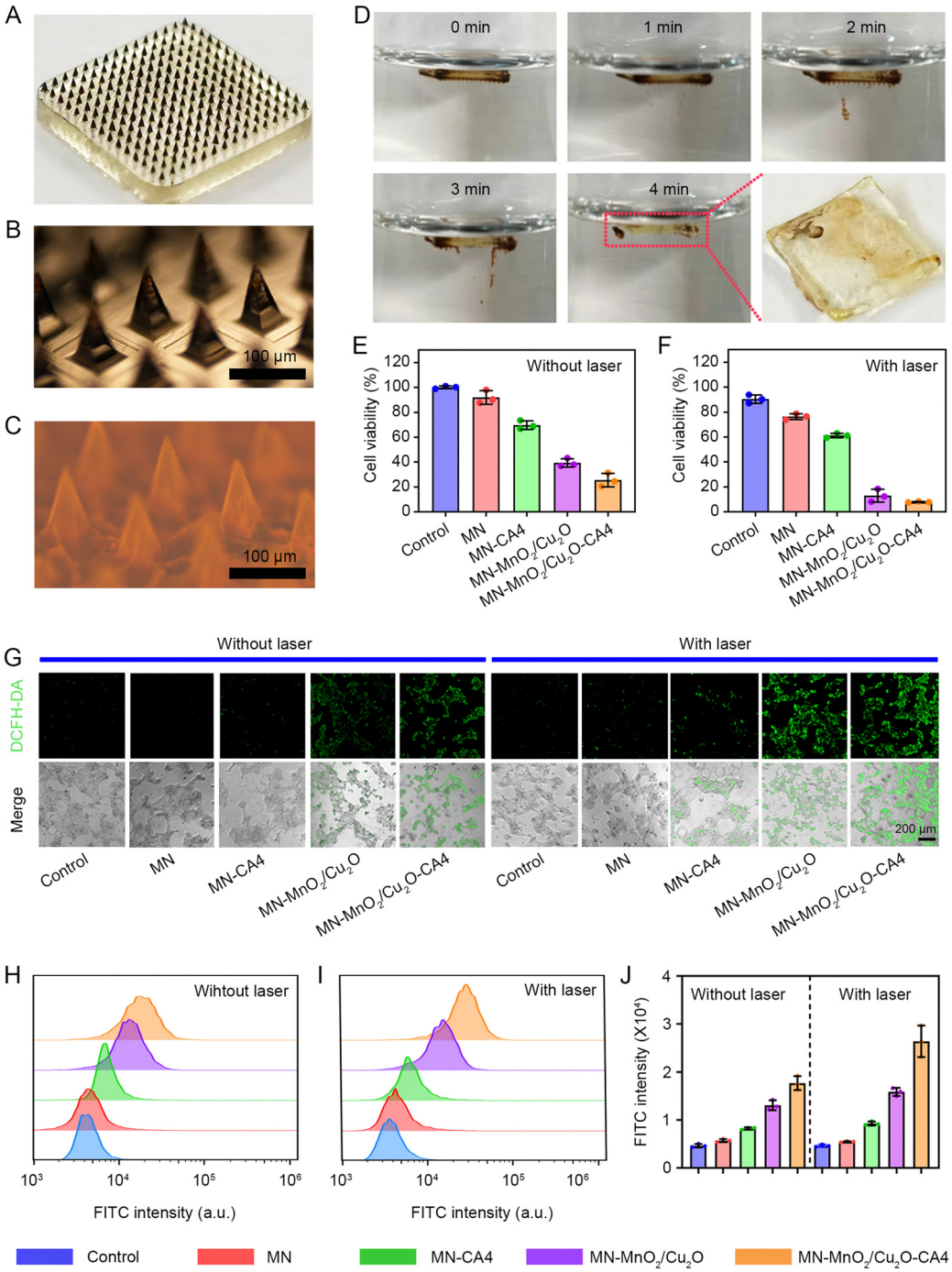

Fig. 3 (A) Representative image of MN-MnO_2/Cu_2O-CA4. (B) Microscope images of MN-MnO_2/Cu_2O-CA4. (C) Fluorescence microscope image of microneedle loaded with rhodamine B. (D) The degradation process of the needle tip of MN-MnO_2/Cu_2O-CA4. (E and F) Cell viability of A431 cells with indicated microneedles without (E) and with (F) laser irradiation. (G) Measurement of ROS generation inside A431 cells with indicated treatments by fluorescence microscope. (H and I) Measurement of ROS generation inside A431 cells treated with indicated microneedles with (H) and without (I) NIR laser irradiation by flow cytometry. (J) The quantitative fluorescence intensity analysis of H and I.

glucose and oxygen into gluconic acid and H_2O_2. Besides, the produced H_2O_2 was dependent on the concentration of glucose. This result was also confirmed by a potassium permanganate-based colorimetric assay (Fig. S1, ESI†). Next, the release behavior of Cu from MnO_2/Cu_2O was investigated. Cu was rapidly released from MnO_2/Cu_2O under acidic conditions, whereas much less Cu was released under neutral conditions (Fig. 2B and Fig. S2, ESI†). Besides, the release behavior of Cu was pH-dependent. Combining the produced H_2O_2 in the presence of glucose and the released Cu, the Fenton-like reaction was initiated to generate hydroxyl radicals, which was assessed by a methylene blue degradation assay.[23] As

shown in Fig. 2C, MnO_2/Cu_2O efficiently degraded methylene blue in the presence of H_2O_2 while MnO_2 showed little effect. In addition, MnO_2/Cu_2O in the presence of both H_2O_2 and glucose displayed the most effective ability to degrade dyes. Collectively, these results demonstrated that MnO_2/Cu_2O could release Cu under acidic conditions, which reacted with the self-supplied H_2O_2 in the presence of glucose to efficiently produce hydroxyl radicals.

The photothermal performance of MnO_2/Cu_2O was also investigated. As photothermal ability is highly associated with light absorption, the absorption properties of MnO_2/Cu_2O was investigated using UV-Vis-NIR spectroscopy.[24] The optical absorption spectra of MnO_2/Cu_2O showed a broad band in the NIR region, which indicated that MnO_2/Cu_2O had good NIR absorption ability (Fig. 2D and Fig. S3, S4, ESI†). The photothermal property of MnO_2/Cu_2O was then studied under the irradiation of an NIR laser. As shown in Fig. 2E, the temperature of a MnO_2/Cu_2O solution at 4 mg/mL under NIR laser irradiation for 10 min reached 59.6 °C, which indicated a good photothermal conversion of MnO_2/Cu_2O. With the increase of either the concentration of MnO_2/Cu_2O or the power of the laser, the temperature of the MnO_2/Cu_2O solution increased (Fig. 2E and F). Moreover, no significant decline in temperature was observed by irradiating the MnO_2/Cu_2O solutions for six on-off cycles, which suggested the stable photothermal effect of MnO_2/Cu_2O (Fig. 2G). The good photothermal effect of MnO_2/Cu_2O was also validated by the infrared thermal images (Fig. 2H).

To promote the penetration of drugs in skin cancer, a microneedle patch was chosen as a noninvasive delivery method.[25–28] MnO_2/Cu_2O nanosheets, together with a vascular disrupting agent CA4 as the representative of small molecule, were loaded on the microneedle patch.[29,30] As shown in Fig. 3A, the MN-MnO_2/Cu_2O-CA4 patch was composed of a series of sharp tips, which were dark brown due to the presence of MnO_2/Cu_2O. Microscope images showed that the MnO_2/Cu_2O-CA4 patch had pyramid-shaped needles with uniform size (Fig. 3B). To confirm CA4 could also be effectively loaded on the MN patch, rhodamine B was chosen as an alternative for easy observation under fluorescence microscopy. A red fluorescence could be observed in the needles of the patch, which indicated that small molecular drugs could be successfully loaded on the MN patch (Fig. 3C). These results indicate that both MnO_2/Cu_2O and small molecules can be successfully loaded onto the MN patch. In addition, the tips of the MN-MnO_2/Cu_2O-CA4 patch could be detached from the patch within 4 min, which indicates a good degradable property (Fig. 3D). These phenomena could facilitate the rapid release of loaded MnO_2/Cu_2O and CA4.

To assess the anticancer effect of the MN-MnO_2/Cu_2O-CA4 patch, the cell counting kit-8 (CCK-8) assay was implemented to measure the cytotoxicity of the MN-MnO_2/Cu_2O-CA4 patch on human cutaneous squamous cell carcinoma A431 cells. As shown in Fig. 3E, the MN patch showed little influence on the cell viability compared to the control group, indicating the good biocompatibility of the MN patch. In contrast, the cell viability of A431 cells treated with MN-CA4 decreased to 69.8%, which indicated that the released CA4 could inhibit cell growth.

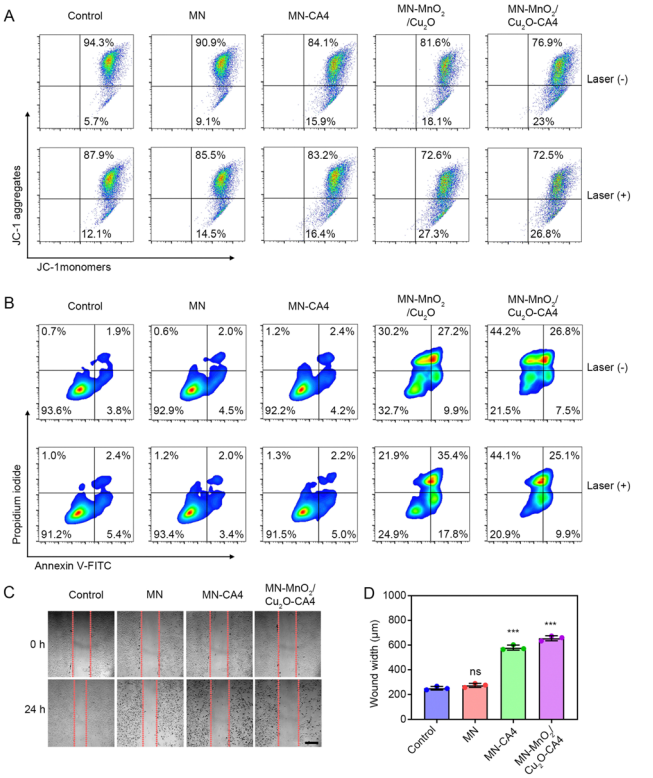

Fig. 4 Anticancer mechanism of MN-MnO_2/Cu_2O-CA4. (A) Measurement of mitochondrial membrane potential in A431 cells after the indicated treatments. (B) Annexin V-FITC/PI apoptosis analyses of A431 cells after the indicated treatments. (C) Cell migration of HUVEC cells with indicated treatments. Scale bar represents 500 μm. (D) The quantitative analysis of wound width for C.

For the A431 cells treated with MN-MnO_2/Cu_2O, cell viability remarkably declined to 39.4%, which was attributed to the hydroxyl radicals produced from the Fenton-like reaction between the released Cu and self-supplied H_2O_2. Of note, the cell viability further decreased to 25.5% after A431 cells were treated with the MN-MnO_2/Cu_2O-CA4 patch. Under the irradiation of NIR laser, the cell viability of the MN-MnO_2/Cu_2O and MN-MnO_2/Cu_2O-CA4 groups decreased to 18.4% and 7.6%, respectively (Fig. 3F). This may be ascribed to the photothermal effect with simultaneously killing cancer cells and promoting the efficiency of the Fenton-like reaction. To validate our hypothesis, cellular ROS levels were determined by staining the cells with the probe 2,7-dichlorodihydrofluorescein diacetate (DCFH-DA). As shown in Fig. 3G, more and stronger green fluorescence was observed in the MN-MnO_2/Cu_2O and MN-MnO_2/Cu_2O-CA4 groups under NIR laser irradiation compared to those without NIR laser irradiation, which indicated the enhanced oxidative stress induced by the photothermal effect. These results were further validated using flow cytometry analysis, which was consistent with the observations from the CCK-8 assay (Fig. 3H–J).

To understand the therapeutic mechanism of the MN-MnO_2/Cu_2O-CA4 patch, changes in the mitochondria membrane potential induced by oxidative stress were evaluated by staining A431 cells

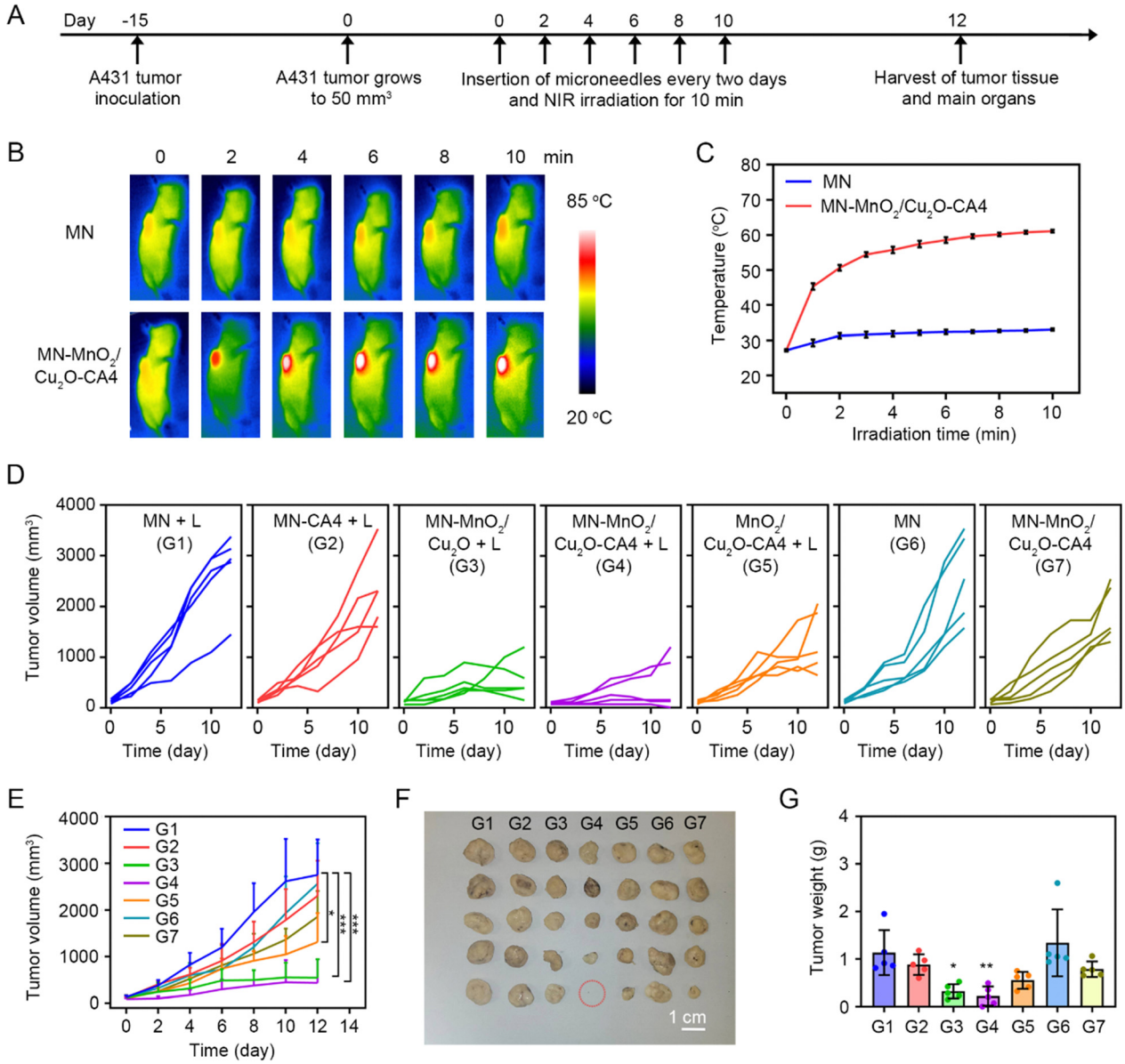

Fig. 5 *In vivo* therapeutic effect of MN-MnO_2/Cu_2O-CA4 on cSCC. (A) The schematic therapeutic schedule process of MN-MnO_2/Cu_2O-CA4 for A431 tumor-bearing mice. (B) Infrared thermal images of tumor-bearing mice with microneedle patch under NIR laser irradiation. (C) Temperature changes of the tumor with indicated treatments under NIR laser irradiation. (D and E) Individual tumor growth curves (D) and tumor volumes (E) of mice with indicated treatments. (F) Photographs of A431 tumors dissected from mice. (G) Weight of A431 tumors at the end of the treatment period.

with a dye JC-1 after treatment by various formulas. As shown in Fig. 4A, MN-CA4 increased the ratio of JC-1 monomer to JC-1 aggregates, which indicated that the mitochondrial membrane potential was attenuated. A previous study has confirmed that mitochondrial elongation occurred during CA4-induced autophagy.[31] Similar results were observed in A431 cells treated with MN-MnO_2/Cu_2O, implying a decrease of membrane potential and mitochondria dysfunction. This result may be ascribed to the increased oxidative stress induced by MN-MnO_2/Cu_2O. A further increase of JC-1 monomer to JC-1 aggregates was observed in A431 cells treated with MN-MnO_2/Cu_2O-CA4. Of note, under the irradiation of NIR laser, the ratio of JC-1 monomer to JC-1 aggregates was higher in A431 cells treated with MN-MnO_2/Cu_2O and MN-MnO_2/Cu_2O-CA4 than that without NIR irradiation. This could be attributed to the enhanced oxidative stress from the photothermal effect-promoted Fenton-like reaction.[32] Furthermore, cell apoptosis was detected by annexin V/PI co-staining. As shown in Fig. 4B, fewer apoptotic cells were observed in MN and MN-CA4 cells compared to the control group. It has been reported that a high concentration of CA4 (5 μM) rather than a low concentration (2 μM) can induce cell apoptosis and the concentration of CA4 used in our study was lower than 2 μM. In contrast, MN-MnO_2/Cu_2O and MN-MnO_2/Cu_2O-CA4 with or without laser irradiation could induce large amounts of apoptotic and necrotic cells. Besides, inhibition of cell migration was observed in the HUVEC cells treated with MN-CA4

and MN-MnO_2/Cu_2O-CA4 (Fig. 4C and D). Collectively, MN-MnO_2/Cu_2O-CA4 could effectively kill cancer cells through synergistic chemodynamic therapy and photothermal therapy.

Encouraged by the good therapeutic effect *in vitro*, the antitumor effect of MN-MnO_2/Cu_2O-CA4 was carried out on the A431 tumor xenograft mouse model.[33] When tumor sizes reached $\sim$50 mm^3, the A431 tumor-bearing mice were treated (Fig. 5A). For the laser irradiation groups, the mice were exposed to a NIR laser for 10 min after insertion of the patches. The localized temperature of the tumor in MN-MnO_2/Cu_2O-CA4 + laser group increased to 61.1 °C after NIR laser irradiation for 10 min (Fig. 5B, C, and Fig. S5, ESI†). Under laser irradiation, MN-MnO_2/Cu_2O with laser group and MN-MnO_2/Cu_2O-CA4 with laser group showed more effective tumor suppression than the other groups (Fig. 5D and E). The high tumor inhibition could be ascribed to the synergistic antitumor effect between chemodynamic therapy and photothermal therapy. By contrast, MN or MN-CA4 under laser irradiation could hardly eradicate tumors. Importantly, MnO_2/Cu_2O-CA4 with laser group and MN-MnO_2/Cu_2O-CA4 exhibited moderate tumor inhibition, suggesting the critical role of the microneedle delivery system and laser irradiation. Besides, no significant changes of body weight were observed, indicating the good biocompatibility of the MN-MnO_2/Cu_2O-CA4 patches (Fig. S6, ESI†). Additionally, no obvious pathological changes were observed in the major organs after the treatments, which suggested that these treatments induced few side effects in the mice. Taken together, these results indicated that the co-delivery of MnO_2/Cu_2O and CA4 *via* a microneedle patch could effectively ablate tumors by disrupting tumor vasculature, self-supplied H_2O_2-enhanced chemodynamic therapy, and photothermal therapy.

3. Conclusion

In summary, an MN-MnO_2/Cu_2O-CA4 patch has been successfully developed for the therapy of cSCC. The prepared MN-MnO_2/Cu_2O-CA4 patch could effectively deliver adequate drugs locally into the tumor sites, which significantly improved the antitumor effect through enhanced chemodynamic therapy and photothermal therapy. Meanwhile, the released CA4 could inhibit cancer cell migration and tumor growth by disrupting tumor vasculature. Both *in vitro* and *in vivo* results demonstrated the good therapeutic effects of the MN-MnO_2/Cu_2O-CA4 patch. In addition, the photothermal effect could promote the efficiency of the Fenton-like reaction while showing little influence on the GOx-like activity of MnO_2/Cu_2O. This study may open avenues for constructing MN-based multimodal treatment for the enhanced therapy of skin cancers.

Author contributions

E.J.: conceptualization, data curation, formal analysis, funding acquisition, project administration, software, supervision, visualization, writing-original draft, review & editing; M.P.: conceptualization, data curation, methodology, investigation, resources, validation, writing-original draft; Y.X.: methodology, investigation, resources; Y.W.: methodology, investigation, resources; F.Z.: methodology, investigation, resources; H.W.: methodology, investigation, resources; M.L.: conceptualization, funding acquisition, methodology, resources, supervision, writing-review & editing; Y.Z.: conceptualization, funding acquisition, methodology, supervision, writing-review & editing; Y.T.: conceptualization, funding acquisition, methodology, resources, supervision, writing-review & editing.

Conflicts of interest

There are no conflicts to declare.

Acknowledgements

This work is supported by the National Key Research and Development Program of China (2019YFA0111300), the National Natural Science Foundation of China (22277155, 52202359, 32001012), the Science and Technology Program of Guangzhou (202102010225, 202102010217, 202102010284), the Guangdong Basic and Applied Basic Research Foundation (2022A1515012253, 2020A1515010305), the China Primary Health Care Foundation (2022-003), the Thousand Talents Plan, and the Guangdong Provincial Pearl River Talents Program (2019QN01Y131, 2021QN02Y141).

References

1 A. Sanchez-Danes and C. Blanpain, *Nat. Rev. Cancer*, 2018, **18**, 549–561.
2 V. Ratushny, M. D. Gober, R. Hick, T. W. Ridky and J. T. Seykora, *J. Clin. Invest.*, 2012, **122**, 464–472.
3 V. Madan, J. T. Lear and R. M. Szeimies, *Lancet*, 2010, **375**, 673–685.
4 N. M. Ioannidis, W. Wang, N. A. Furlotte, D. A. Hinds, C. D. Bustamante, E. Jorgenson, M. M. Asgari, A. S. Whittemore and A. R. Team, *Nat. Commun.*, 2018, **9**, 4264.
5 K. D. Brantsch, C. Meisner, B. Schonfisch, B. Trilling, J. Wehner-Caroli, M. Rocken and H. Breuninger, *Lancet Oncol.*, 2008, **9**, 713–720.
6 F. F. Gellrich, S. Huening, S. Beissert, T. Eigentler, E. Stockfleth, R. Gutzmer and F. Meier, *J. Eur. Acad. Dermatol. Venereol.*, 2019, **33**, 38–43.
7 C. A. Morton, R. M. Szeimies, N. Basset-Seguin, P. G. Calzavara-Pinton, Y. Gilaberte, M. Haedersda, G. F. L. Hofbauer, R. E. Hunger, S. Karrer, S. Piaserico, C. Ulrich, A. M. Wennberg and L. R. Braathen, *J. Eur. Acad. Dermatol. Venereol.*, 2020, **34**, 17–29.
8 U. Keyal, A. K. Bhatta, G. L. Zhang and X. L. Wang, *J. Am. Acad. Dermatol.*, 2019, **80**, 765–773.
9 Z. M. Tang, P. R. Zhao, H. Wang, Y. Y. Liu and W. B. Bu, *Chem. Rev.*, 2021, **121**, 1981–2019.
10 S. Wang, R. Tian, X. Zhang, G. H. Cheng, P. Yu, J. Chang and X. Y. Chen, *Adv. Mater.*, 2021, **33**, 2007488.

11 W. T. Dang, W. C. Chen, E. G. Ju, Y. T. Xu, K. Li, H. X. Wang, K. Wang, S. X. Lv, D. Shao, Y. Tao and M. Q. Li, *J. Nanobiotechnol.*, 2022, **20**, 1–20.
12 Z. M. Tang, Y. Y. Liu, M. Y. He and W. B. Bu, *Angew. Chem., Int. Ed.*, 2019, **58**, 946–956.
13 S. T. Gao, Y. Jin, K. Ge, Z. H. Li, H. F. Liu, X. Y. Dai, Y. H. Zhang, S. Z. Chen, X. J. Liang and J. C. Zhang, *Adv. Sci.*, 2019, **6**, 1902137.
14 L. S. Lin, T. Huang, J. B. Song, X. Y. Ou, Z. T. Wang, H. Z. Deng, R. Tian, Y. J. Liu, J. F. Wang, Y. Liu, G. C. Yu, Z. J. Zhou, S. Wang, G. Niu, H. H. Yang and X. Y. Chen, *J. Am. Chem. Soc.*, 2019, **141**, 9937–9945.
15 M. Zhang, R. X. Song, Y. Y. Liu, Z. G. Yi, X. F. Meng, J. W. Zhang, Z. M. Tang, Z. W. Yao, Y. Liu, X. G. Liu and W. B. Bu, *Chem-Us*, 2019, **5**, 2171–2182.
16 L. S. Lin, J. F. Wang, J. B. Song, Y. J. Liu, G. Z. Zhu, Y. L. Dai, Z. Y. Shen, R. Tian, J. Song, Z. T. Wang, W. Tang, G. C. Yu, Z. J. Zhou, Z. Yang, T. Huang, G. Niu, H. H. Yang, Z. Y. Chen and X. Y. Chen, *Theranostics*, 2019, **9**, 7200–7209.
17 L. H. Fu, C. Qi, J. Lin and P. Huang, *Chem. Soc. Rev.*, 2018, **47**, 6454–6472.
18 W. Tang, W. P. Fan, W. Z. Zhang, Z. Yang, L. Li, Z. T. Wang, Y. L. Chiang, Y. J. Liu, L. M. Deng, L. C. He, Z. Y. Shen, O. Jacobson, M. A. Aronova, A. Jin, J. Xie and X. Y. Chen, *Adv. Mater.*, 2019, **31**, 1900401.
19 Y. Y. Huang, J. S. Ren and X. G. Qu, *Chem. Rev.*, 2019, **119**, 4357–4412.
20 M. R. Peng, E. G. Ju, Y. T. Xu, Y. Q. Wang, S. X. Lv, D. Shao, H. X. Wang, Y. Tao, Y. Zheng and M. Q. Li, *NPG Asia Mater.*, 2022, **14**, 95.
21 D. W. Jiang, D. L. Ni, Z. T. Rosenkrans, P. Huang, X. Y. Yan and W. B. Cai, *Chem. Soc. Rev.*, 2019, **48**, 3683–3704.
22 Y. P. Gao, L. B. Wang, Z. Y. Li, A. G. Zhou, Q. K. Hu and X. X. Cao, *Solid State Sci.*, 2014, **35**, 62–65.
23 W. T. Dang, Y. Q. Wang, W. C. Chen, E. G. Ju, R. L. Mintz, Y. Teng, L. L. Zhu, K. Wang, S. X. Lv, H. F. Chan, Y. Tao and M. Q. Li, *ACS Appl. Mater. Interfaces*, 2023, **4**, 4911–4923.
24 Y. Tao, H. F. Chan, B. Y. Shi, M. Q. Li and K. W. Leong, *Adv. Funct. Mater.*, 2020, **30**, 2005029.
25 Y. Q. Ye, J. C. Yu, D. Wen, A. R. Kahkoska and Z. Gu, *Adv. Drug Delivery Rev.*, 2018, **127**, 106–118.
26 C. Wang, Y. Q. Ye, G. M. Hochu, H. Sadeghifar and Z. Gu, *Nano Lett.*, 2016, **16**, 2334–2340.
27 G. He, Y. S. Li, M. R. Younis, L. H. Fu, T. He, S. Lei, J. Lin and P. Huang, *Nat. Commun.*, 2022, **13**, 6238.
28 Y. Zhang, Y. Xu, H. Kong, J. Zhang, H. F. Chan, J. Wang, D. Shao, Y. Tao and M. Li, *Exploration*, 2023, **3**, 20210170.
29 Y. Q. Fang, Z. Liu, H. X. Wang, X. Luo, Y. T. Xu, H. F. Chan, S. X. Lv, Y. Tao and M. Q. Li, *ACS Appl. Mater. Interfaces*, 2022, **14**, 27525–27537.
30 S. C. Yang, Z. H. Tang, C. Y. Hu, D. W. Zhang, N. Shen, H. Y. Yu and X. S. Chen, *Adv. Mater.*, 2019, **31**, 1805955.
31 L. M. Greene, N. M. O'Boyle, D. P. Nolan, M. J. Meegan and D. M. Zisterer, *Biochem. Pharmacol.*, 2012, **84**, 612–624.
32 X. Q. Yu, Q. Su, X. W. Chang, K. Chen, P. Y. Yuan, T. Liu, R. Tian, Y. K. Bai, Y. M. Zhang and X. Chen, *Biomaterials*, 2021, **278**, 121181.
33 M. A. Burgo, N. Roudiani, J. Chen, A. L. Santana, N. Doudican, C. Proby, D. Felsen and J. A. Carucci, *JCI Insight*, 2018, **3**, e120750.

